

The CARMENES search for exoplanets around M dwarfs

The He I infrared triplet lines in PHOENIX models of M2–3 V stars

D. Hintz¹, B. Fuhrmeister¹, S. Czesla¹, J. H. M. M. Schmitt¹, A. Schweitzer¹, E. Nagel², E. N. Johnson³, J. A. Caballero⁴, M. Zechmeister³, S. V. Jeffers³, A. Reiners³, I. Ribas^{5,6}, P. J. Amado⁷, A. Quirrenbach⁸, G. Anglada-Escudé^{7,9}, F. F. Bauer⁷, V. J. S. Béjar^{10,11}, M. Cortés-Contreras⁴, S. Dreizler³, D. Galadí-Enríquez¹², E. W. Guenther^{2,10}, P. H. Hauschildt¹, A. Kaminski⁸, M. Kürster¹³, M. Lafarga^{5,6}, M. López del Fresno⁴, D. Montes¹⁴, and J. C. Morales^{5,6}

¹ Hamburger Sternwarte, University of Hamburg, Gojenbergsweg 112, D-21029 Hamburg, Germany
e-mail: dominik.hintz@hs.uni-hamburg.de

² Thüringer Landessternwarte Tautenburg, Sternwarte 5, D-07778 Tautenburg, Germany

³ Institut für Astrophysik, Friedrich-Hund-Platz 1, D-37077 Göttingen, Germany

⁴ Centro de Astrobiología (CSIC-INTA), ESAC, Camino Bajo del Castillo s/n, E-28692 Villanueva de la Cañada, Madrid, Spain

⁵ Institut de Ciències de l'Espai (ICE, CSIC), Campus UAB, c/ de Can Magrans s/n, E-08193 Bellaterra, Barcelona, Spain

⁶ Institut d'Estudis Espacials de Catalunya (IEEC), E-08034 Barcelona, Spain

⁷ Instituto de Astrofísica de Andalucía (CSIC), Glorieta de la Astronomía s/n, E-18008 Granada, Spain

⁸ Landessternwarte, Zentrum für Astronomie der Universität Heidelberg, Königstuhl 12, D-69117 Heidelberg, Germany

⁹ School of Physics and Astronomy, Queen Mary, University of London, 327 Mile End Road, London, E1 4NS, UK

¹⁰ Instituto de Astrofísica de Canarias, c/ Vía Láctea s/n, E-38205 La Laguna, Tenerife, Spain

¹¹ Departamento de Astrofísica, Universidad de La Laguna, E-38206 Tenerife, Spain

¹² Centro Astronómico Hispano-Alemán (MPG-CSIC), Observatorio Astronómico de Calar Alto, Sierra de los Filabres, E-04550 Gérgal, Almería, Spain

¹³ Max-Planck-Institut für Astronomie, Königstuhl 17, D-69117 Heidelberg, Germany

¹⁴ Departamento de Física de la Tierra y Astrofísica and UPARCOS-UCM (Unidad de Física de Partículas y del Cosmos de la UCM), Facultad de Ciencias Físicas, Universidad Complutense de Madrid, E-28040, Madrid, Spain

Received 28 January 2020 / accepted dd mm 2020

ABSTRACT

The He I infrared (IR) line at a vacuum wavelength of 10833 Å is a diagnostic for the investigation of atmospheres of stars and planets orbiting them. For the first time, we study the behavior of the He I IR line in a set of chromospheric models for M-dwarf stars, whose much denser chromospheres may favor collisions for the level population over photoionization and recombination, which are believed to be dominant in solar-type stars. For this purpose, we use published PHOENIX models for stars of spectral types M2 V and M3 V and also compute new series of models with different levels of activity following an ansatz developed for the case of the Sun. We perform a detailed analysis of the behavior of the He I IR line within these models. We evaluate the line in relation to other chromospheric lines and also the influence of the extreme ultraviolet (EUV) radiation field. The analysis of the He I IR line strengths as a function of the respective EUV radiation field strengths suggests that the mechanism of photoionization and recombination is necessary to form the line for inactive models, while collisions start to play a role in our most active models. Moreover, the published model set, which is optimized in the ranges of the Na I D₂, H α , and the bluest Ca II IR triplet line, gives an adequate prediction of the He I IR line for most stars of the stellar sample. Because especially the most inactive stars with weak He I IR lines are fit worst by our models, it seems that our assumption of a 100% filling factor of a single inactive component no longer holds for these stars.

Key words. stars: activity – stars: chromospheres – stars: late-type

1. Introduction

Spectral lines arising in a stellar chromosphere provide essential information on stellar activity. In the optical wavelength range, widely used chromospheric indicator lines include the Ca II H and K lines (3934.77 Å, 3969.59 Å), the He I D₃ line (5877.25 Å), the Na I D doublet (5897.56 Å, 5891.58 Å), and the H α (6564.62 Å) line. In the infrared, the Ca II infrared triplet (IRT) lines (8500.35 Å, 8544.44 Å, 8664.52 Å) and the He I IRT lines (hereafter He I IR line for short) at 10833 Å are widely

used chromospheric diagnostics.¹ Specifically, the He I IR line has recently become even more important in the light of investigations of exoplanet atmospheres around late-type stars (e.g., Spake et al. 2018; Nortmann et al. 2018; Salz et al. 2018). For this reason, it is imperative to improve our understanding of the He I IR line behavior of stars, especially for the very late-type stars. In this paper, we investigate the behavior of the He I IR line in early M-dwarf stars.

¹ We use vacuum wavelengths throughout the paper. However, the He I IR line is well known for its air wavelength at 10830 Å.

The He I IR line is a triplet line of orthohelium, whose three components are centered at 10 832.057, 10 833.217, and 10 833.306 Å. The term scheme of the neutral helium atom splits into the ortho- and parahelium branch, depending on whether the electrons have aligned or opposite spins. Singlet lines only occur in parahelium, while orthohelium is characterized by triplet lines.

The lower level of the He I IR line is the metastable 2^3S level of orthohelium, which is located about 20 eV above the ground state of (para-)helium. The He I IR line appears in absorption when the occupation number of the metastable level is higher than that of the overlying 2^3P triplet levels, and vice versa for an emission line. A decisive question is which process is responsible for populating the metastable ground state. Previous studies modeling the He I IR line (e.g., Andretta & Giampapa 1995; Andretta & Jones 1997) investigated two possible line formation mechanisms in detail: (i) the photoionization and recombination (PR) mechanism, and (ii) collisional excitation.

In the PR formation scenario, the continuum shortward of 504 Å is important for photoionization of He I in the ground state. The photons from this continuum, produced in the transition region and corona, photoionize the He I atoms and produce free electrons. These can be captured by the helium ion into a highly excited energy level, from which they finally cascade down to the metastable 2^3S level. The excited He I atom then interacts with photospheric photons. The PR mechanism is thought to dominate the population of the metastable level at temperatures below 10 000 K in the upper chromosphere. In the collisional line formation scenario, a helium atom in the ground state is excited by an electron collision to the 2^3S level. This process requires a sufficiently dense high-energy electron population, which is typically only encountered in the hot upper chromosphere and lower transition region at temperatures above 20 000 K.

Vaughan & Zirin (1968) were the first to study the He I IR line in stars of spectral type between F and M. In their study, He I IR absorption was detected for most of the G and early K-type stars in their sample. Further observations by Zirin (1975a) revealed He I IR emission lines for some late M-type stars. Zirin (1975b) constructed a solar model incorporating the PR mechanism and concluded that this mechanism is decisive for the formation of the He I D₃ and He I IR lines. Furthermore, they postulated a correlation between the He I IR line equivalent widths and the soft X-ray flux for stars that show the line in absorption. This was later observed by Zarro & Zirin (1986) for stars in the spectral range between F7 and K3.

In a study of the formation of the He I IR line in the Sun, Avrett et al. (1994) generated different solar models based on the VAL C model by Vernazza et al. (1981) for the average quiet Sun. In varying the atmospheric height of the transition region onset as well as changing the incident radiation from the transition region, Avrett et al. (1994) found that enhancing the radiation leads to an increase in absorption of the solar He I IR line. In contrast, a solar plage model, characterized by a radiation level thrice that of the quiet Sun and a transition region moved inward, showed a slightly weaker He I IR line than the average quiet model. The authors attributed the weakening of the line strength in the plage model to its high density and to the relatively lower geometric extension of the chromosphere in this model. Andretta & Giampapa (1995) found a clear correlation between the X-ray emission and the neutral helium lines in chromospheric models of F, G, and early K stars by investigating the behavior of the He I D₃ and He I IR line with the VAL C model shifted in density. Intensifying the ionizing radiation field

leads to stronger He I IR line absorption until a limit of ~ 400 mÅ in the equivalent width is reached. Then the behavior reverses and the line tends to go into emission. Studying the He I IR line of stars of spectral types G, K, and M, Sanz-Forcada & Dupree (2008) concluded that the collisional excitation mechanism may contribute to the line formation for active dwarfs because high densities of neutral helium in the upper chromosphere can be reached. This conclusion agrees with the results of Andretta & Giampapa (1995).

Andretta & Jones (1997) theoretically studied the effects of these two He I IR line formation mechanisms on the solar spectrum. From computing a series of solar models that varied in density and radiation field, they found that the formation mechanisms influence the He I IR line quite differently. While the He I IR line is highly sensitive to irradiation from the transition region and corona in the classical VAL C model for the quiet Sun, collisions become more important when the chromospheric structure is shifted inward toward increasing densities. After an inward shift of ten times the mass load above the quiet-Sun model, the line becomes almost insensitive to the radiation field. Further shifting toward higher densities drives the line into emission. Later, Leenaarts et al. (2016) investigated the spatial structure of the He I IR line using a three-dimensional radiation-magnetohydrodynamic simulation. From their model atmosphere, which included the solar chromosphere and corona, they were able to confirm that the PR mechanism is responsible for populating the 2^3S level in the case of the Sun. Compared to this, the collisional excitation appeared to be negligible. However, they also found that variations of the chromospheric electron density have a crucial effect on variations of the He I IR line.

The number of He I IR line studies in M dwarfs falls far short of that carried out for solar-type stars. A recent observational study by Fuhrmeister et al. (2019) used high-resolution infrared spectra obtained with the Calar Alto high-Resolution search for M dwarfs with Exo-earths with Near-infrared and optical Echelle Spectrographs (CARMENES; Quirrenbach et al. 2018) to examine the behavior of the He I IR line in M dwarfs. They found the line to be prominent in early M dwarfs with a tendency to decrease in strength toward later spectral types. Moreover, the line was observed transiently in emission during flaring events. Fuhrmeister et al. (2019) was unable to detect a correlation of the line strength measured by its pseudo-equivalent width (pEW) and the fractional X-ray luminosity (L_X/L_{bol}) even for the earliest M dwarfs. It remains unclear whether this noncorrelation is caused by observational deficits (e.g., the lack of simultaneous observations) or a stronger effect of the collisional level population mechanism. Hintz et al. (2019) compared models of optical chromospheric lines with observed spectra of a stellar sample of M2–3 V stars. In the best-fit models, the onset of the transition region can reach column mass densities more than one magnitude higher than the density of the solar VAL C model even in the low-activity regime, implying much higher electron densities than in the Sun. Even in early M dwarfs, collisions may therefore play a larger role in the He I IR line formation. For this reason, chromospheric models dedicated to M dwarfs need to be computed to theoretically explain the observed behavior.

In this study, we investigate the behavior of the He I IR line using a model set of chromospheres based on the model set presented by Hintz et al. (2019). We introduce the model set as well as the comparison observations, and describe the method of measuring the equivalent widths in Sect. 2. In Sect. 3 we show and discuss our results, and we present our conclusions in Sect. 4.

2. Models and observations

2.1. Observations and stellar sample

The observed spectra to which we compared our models were taken with the CARMENES spectrograph (Quirrenbach et al. 2018) and retrieved from the CARMENES archive; the CARMENES spectrograph covers the He I IR line in its near-infrared channel (NIR), which ranges from 9600 to 17 100 Å with a resolution of $R = 80\,400$. All spectra were reduced by the CARMENES data reduction pipeline (Caballero et al. 2016; Zechmeister et al. 2018).

For further correction and averaging of the spectra, we followed the same procedures as Fuhrmeister et al. (2019): The stellar spectra were corrected for telluric contamination using the method of Nagel (2019) and for airglow lines by coadding the spectra using the SpEctrum Radial Velocity AnaLyser (SERVAL, Zechmeister et al. 2018). Furthermore, barycentric and radial velocity shifts were corrected in the spectra.

We compared the model set to 50 M2–3 V stars, which are a subsample of the stars used by Fuhrmeister et al. (2019). Our sample is defined by the effective temperature range $T_{\text{eff}} = 3500 \pm 50$ K, and has previously been investigated by Hintz et al. (2019). It comprises four active stars in which the lines of Na I D₂, H α , and the Ca II IRT lines usually appear in emission; for further details about the stellar parameters of the sample, we refer to Table 1 in Hintz et al. (2019).

2.2. Measuring the He I IR line pseudo-equivalent width

To characterize the line strengths in the investigated spectra, we calculated the pEW with the same ansatz as Fuhrmeister et al. (2019), who fit Voigt profiles to the He I IR line profiles. This line profile fitting has a long tradition. It has also been performed, for example, by Takeda & Takada-Hidai (2011) using Gaussian models to estimate the equivalent width of the He I IR line in late-type stars.

In the following, we give a brief overview of the method and refer to Fuhrmeister et al. (2019) for more details. We used an empirical function consisting of four Voigt profiles to approximate the spectrum in the wavelength range of 10 829–10 835 Å. The Voigt components represent the relevant spectral lines, including the He I IR line. The two red components of the He I IR triplet at 10 833.217 and 10 833.306 Å are unresolved, and, therefore, represented by one Voigt profile centered at 10 833.25 Å, which is used to estimate the pEW. The weak blue triplet component is neglected in the calculations of this pEW because it is blended with an unidentified absorption line. Figure 1 shows the Voigt profile fits of the He I IR line for three model spectra of different states of activity. While the fit of the more or less filled-in line (middle panel) hardly reproduces the shape of the line, clear absorption and emission lines (top and bottom panels, respectively) are well fit by the respective Voigt profiles. Therefore, pEW values close to zero may be problematic.

To determine the pEW of the H α , He I D₃, Na I D₂, and the bluest Ca II IRT line, we integrated the model spectrum in the respective wavelength ranges following Fuhrmeister et al. (2019) for the stellar sample. The central wavelengths of the lines, the line widths, and the ranges of the reference bands are adopted from Fuhrmeister et al. (2019).

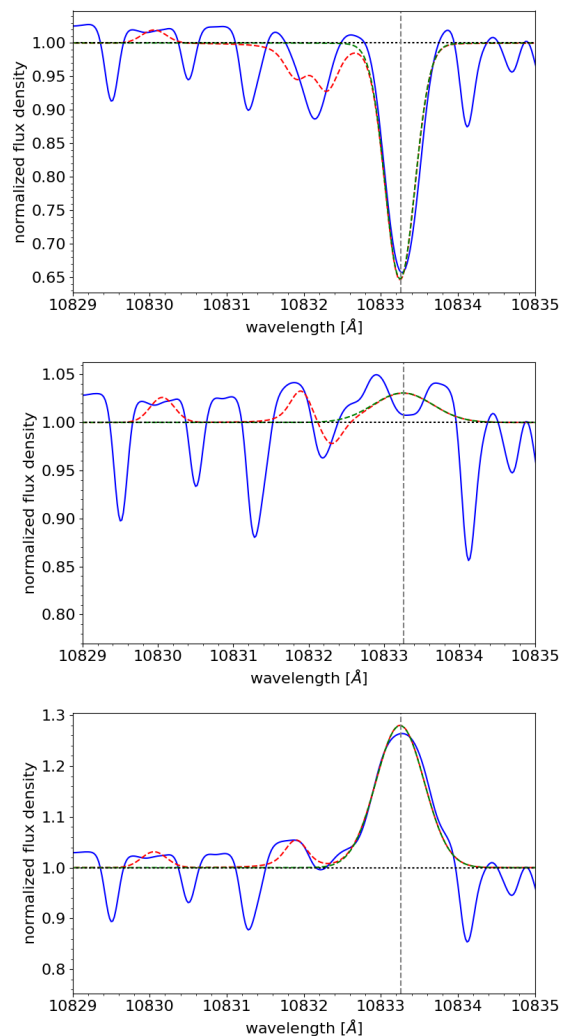


Fig. 1. Fitting Voigt profiles in the wavelength range around the He I IR triplet (10 829–10 835 Å). Three models (solid blue lines) at different states of activity are shown: a model with He I IR in absorption (*top panel*, number 042 from Hintz et al. (2019)) or number A2 from the model series A, details are given in Sect. 2.4), one nearly filled in (*middle panel*, number 149), and one with the line in emission (*bottom panel*, number 121). The red dashed line is the best fit of four Voigt profiles in the wavelength range of 10 829–10 835 Å. The dashed green line represents the single Voigt profile fit to the center of the two indistinguishable red components of the He I IR triplet at 10 833.25 Å (dashed vertical line). The pEW of the He I IR line is calculated from the green Voigt profile.

2.3. Previous chromospheric models

The stellar atmosphere code PHOENIX² has been developed for calculations of atmospheres and spectra from various objects such as stars, planets, novae, and supernovae (Hauschildt 1992, 1993; Hauschildt & Baron 1999). A recent library of PHOENIX model photospheres was calculated by Husser et al. (2013) in the effective temperature range of 2 300–12 000 K, covering a wide range of different stellar spectral types. Based on one of these photospheric models, Hintz et al. (2019) computed chromosphere models for M dwarfs using the PHOENIX code, but extending the photospheric PHOENIX model, which was com-

² <https://www.physik.uni-hamburg.de/en/hs/group-hauschildt/research/phoenix.html>

Table 1. Parameters of the extended model series A and B based on models 042 and 080 from Hintz et al. (2019), hereafter A2 and B4 in the new model series, respectively.

Model	m_{\min}^a [dex]	m_{mid}^a [dex]	T_{mid}^a [K]	m_{top}^a [dex]	T_{top}^a [K]	∇_{TR}^a [dex]	m_i/m_0^b
A1	-3.0	-4.1	5500	-5.5	6500	7.5	0.37
A2	-2.5	-3.6	5500	-5.0	6500	7.5	1.0
A3	-2.0	-3.1	5500	-4.5	6500	7.5	3.16
A4	-1.9	-3.0	5500	-4.4	6500	7.5	4.47
B1	-2.5	-3.5	5500	-5.0	7500	8.5	0.1
B2	-2.3	-3.3	5500	-4.8	7500	8.5	0.16
B3	-1.8	-2.8	5500	-4.3	7500	8.5	0.50
B4	-1.5	-2.5	5500	-4.0	7500	8.5	1.0
B5	-1.3	-2.3	5500	-3.8	7500	8.5	1.59
B6	-1.2	-2.2	5500	-3.7	7500	8.5	2.24

^a The six parameters are consistent with the definitions of Hintz et al. (2019). The column mass density m_{\min} represents the onset of the lower chromosphere and also marks the location of the temperature minimum. The end of the lower chromosphere is located at the column mass density m_{mid} and the temperature T_{mid} . The end of the upper chromosphere and onset of the transition region is located at $(m_{\text{top}}, T_{\text{top}})$, and ∇_{TR} gives the temperature gradient of the transition region.

^b The parameter m_i/m_0 defines the mass load in comparison to the respective basis model.

puted by Husser et al. (2013) with $T_{\text{eff}} = 3500$ K, $\log g = 5.0$ dex, $[\text{Fe}/\text{H}] = 0.0$ dex, and $[\alpha/\text{Fe}] = 0.0$ dex, by a chromosphere and transition region, assuming a temperature structure characterized by linear sections in the logarithm of the column mass density for the lower and upper chromosphere as well as for the transition region. In total, we varied six free parameters in the temperature structure of the chromosphere and computed a set of 166 one-dimensional spherically symmetric chromospheric models. In creating the models, the semi-empirical, solar VAL C temperature structure was parameterized and adjusted to the M-dwarf sample. The parameterized ad hoc temperature structure represents the unknown heating mechanisms in the upper atmosphere. In addition, we assumed hydrostatic equilibrium and neglected any acoustic and magnetic waves. Convergence was achieved using nonlocal thermodynamic equilibrium (NLTE) calculations for the chromospheric lines. The grid encompasses models of various levels of activity. The spectra of the inactive models typically show the chromospheric lines in absorption, while with increasing activity, the lines go into emission. Hintz et al. (2019) optimized their models to simultaneously fit the Na I D₂, H α , and the bluest Ca II IRT line of the stellar sample described above.

2.4. Construction of new chromospheric models

Here we extend our previous study that we performed in Hintz et al. (2019) by constructing two series of models with the specific goal of studying the behavior of the He I IR line in terms of the activity state. We varied the activity level of a given chromospheric temperature structure by shifting the whole density structure. Models shifted farther inward toward higher densities correspond to higher activity states. In particular, we performed systematic density shifts for two inactive best-fit models of Hintz et al. (2019), those designated numbers 042 and 080 therein.

The temperature structure of these two models was shifted toward higher and lower densities following the approach of Andretta & Jones (1997). Table 1 lists the model parameters, and Fig. 2 depicts the temperature structures of these series of models. The change in the column mass density is described by

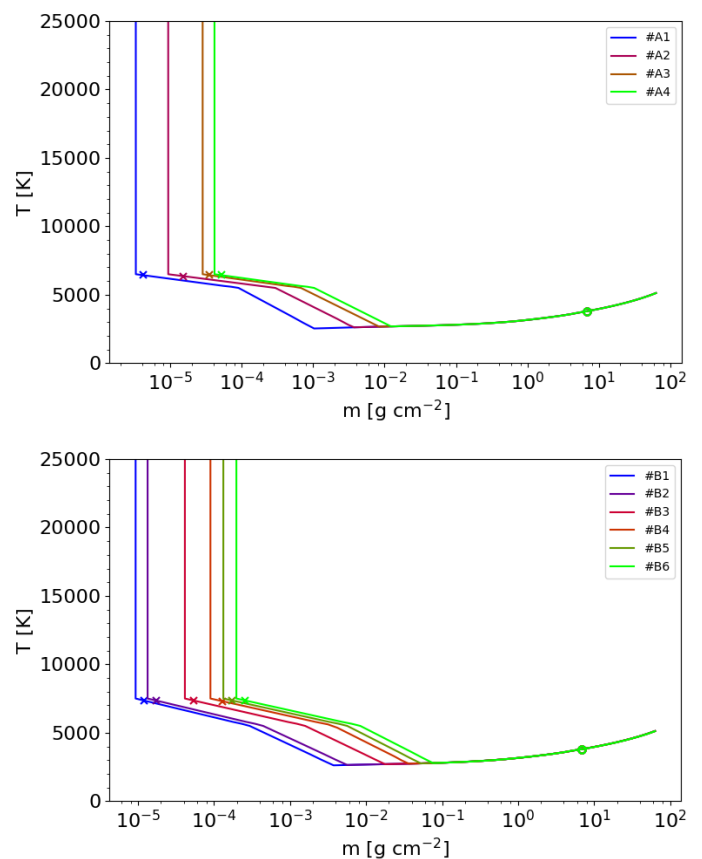


Fig. 2. Model temperature profiles as a function of the column mass densities. The respective model parameters are given in Table 1. The temperature structures of series A are shown in the *top panel*, and those of series B are depicted in the *bottom panel*. Models A2 and B4 in these series correspond to models 042 and 080 from Hintz et al. (2019), respectively. In both series, we also mark the structural positions where the He I IR line core (crosses) and continuum at $\lambda = 10834.5$ Å (open circles) approach an optical depth of $\tau = 1$, i. e., where both become optically thick.

m_i/m_0 relative to the basis model 042, hereafter called model A2 within the new series designated by A, while former model 080 is hereafter called model B4 in series B. Model A1 (blue line in Fig. 2) of the A series represents the least active state with the column mass density of the layers being about ten times lower than that of the original model A2. Model A4 (green line) has the largest inward shift ($m_i/m_0 = 4.47$), corresponding to the highest activity state of the series.

Because we shifted the atmospheric structure on a given discontinuous column mass grid, we obtained deviations in the gradients of the different linear sections. We allowed a tolerance deviation at maximum of 15% for the gradients compared to the gradients of the respective basis model. Therefore the series are not equidistant on the column mass grid. While the NLTE level occupation numbers of the models in series A and B converge during the iteration process of the model computation as described in Hintz et al. (2019), further inward shifts of the innermost models come along with nonconverged atmospheres. Thus, models A4 and B6 yield the limit of the inward density shift of the respective series.

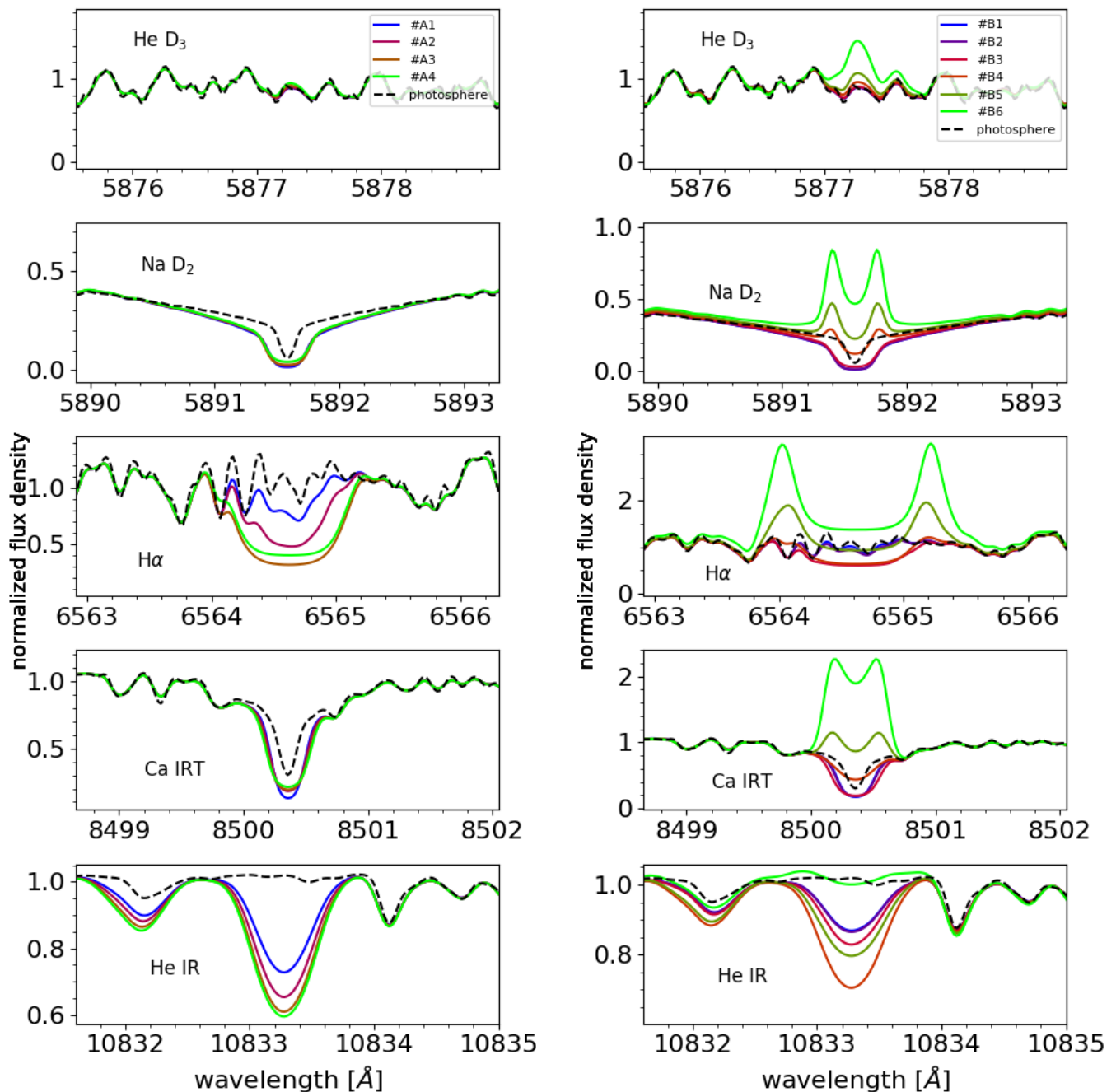


Fig. 3. Spectra according to the temperature structures of the new series A (*left panel*) and B (*right panel*) of models in Fig. 2 (corresponding color-coding) in the spectral ranges of He I D₃, Na I D₂, H α , the bluest Ca II IRT line, and the He I IR line (from *top to bottom*). For comparison, the underlying photosphere model ($T_{\text{eff}} = 3500$ K, $\log g = 5.0$ dex, $[\text{Fe}/\text{H}] = 0.0$ dex, $[\alpha/\text{Fe}] = 0.0$ dex) is plotted as well. The photosphere is taken from Husser et al. (2013).

2.5. New model spectra

From both new series A and B of model atmospheres as given by the chromospheric temperature structures in Fig. 2 we obtained model spectra that are shown in the wavelength ranges of the chromospheric lines of He I D₃, Na I D₂, H α , the bluest Ca II IRT line, and the He I IR line in Fig. 3. The series show the evolution of these chromospheric lines with increasing activity, that is, the inward shifting of the models. The outermost models with the respective lowest densities, A1 and B1, already show absorption in the He I IR line. Models representing higher activity levels lead to an increase in absorption strength, with

model A4 exhibiting the strongest absorption line in series A. In series B, model B4 displays the highest absorption depth, while for models B5 and B6, the He I IR line fills in. In Fig. 2 we also indicate where the He I IR line core and neighboring continuum become optically thick. The corresponding temperatures for the He I IR line core range between 6350 K and 6450 K for series A and between 7300 K and 7400 K for series B. The continuum temperatures are in both cases at ~ 3800 K. The optically thick temperature regions of the line core indicate a He I IR line formation in the upper chromosphere. Furthermore, we determined whether geometric effects caused by the chromospheric exten-

sion above the photosphere contribute to the He I IR line formation in our spherically symmetric models. We were unable to find significant geometric effects with respect to the He I IR line formation.

A comparable behavior is observed in the H α line, where model A4 already shows fill-in. This means that the evolution of H α seems to be shifted compared to that of the He I IR line in series A. In series B, model B3 displays maximum absorption in H α and model B4 just starts to fill in, which is slightly more strongly visible in the wings. In models B5 and B6, the H α line tends to go into emission. However, the H α lines of models B5 and especially B6 exhibit strong trough-like self-absorption features, suggesting that at least model B6 does not represent a real stellar spectrum because even during flares no such broad self-absorption troughs have been observed. This demonstrates that not every parameterized chromosphere leads to realistic spectra.

The He I D₃ line is not visible at all in series A. Only in series B does the line arise beyond the continuum when the activity levels increase: model B5 shows the line in slight emission, and a clear He I D₃ emission line appears in model B6. In the cases of the Na I D₂ and the bluest Ca II IRT line, the evolution is different than in the other cases: the lines start at a maximum absorption depth and fill in for both series while shifting the whole atmospheric structure farther inward. For series B, the response of the lines is again stronger, and for the two innermost models B5 and B6, these lines go into emission.

2.6. Flare classification and model selection

In our investigation of the formation of He I IR line, we focused on quiet atmospheres. Therefore we identified models representing high-activity states (flaring). To that end, we followed observational findings in the spectra. Because H α can be observed in emission during the quiescent state, the line is not well suited as a flare criterion; the same applies for most chromospheric lines in the optical. In contrast, we are not aware of Paschen emission line observations outside of flares, while the line was observed in emission during M-dwarf flares (Schmidt et al. 2012; Fuhrmeister et al. 2008; Liebert et al. 1999; Paulson et al. 2006). Therefore we used the Pa β emission as a discriminator for flaring activity. With this criterion, we identified the highest activity states.

In particular, we computed the pEW for Pa β at 12821.57 Å. For the line core, we assumed a width of 0.5 Å, and the reference bands were located at $12\,811.5 \pm 1.0$ Å and $12\,826 \pm 1.0$ Å. Each model yielding a pEW value below -0.02 Å was considered a flare model and was omitted in the detailed analysis of the He I IR line. One model (number 166 from Hintz et al. 2019) passed this criterion, but the Pa β line developed broad emission wings that reached into the reference bands. Including this model, a total of 81 models were flagged as flaring and were excluded from further consideration.

We also neglected models with a transition region onset below 6000 K. It might be argued that the onset of the transition region occurs where hydrogen becomes completely ionized and hence no longer is an efficient cooling agent. While this occurs only at about 8000 K, hydrogen becomes partially ionized above 5000 K so that cooling starts to diminish (Ayres 1979).

In total, we investigated a subsample of 58 models from Hintz et al. (2019) that fulfilled our selection criteria for inactive chromospheres; these models and the parameter configurations are listed in Table A. Because we are interested in investigating nonflaring models and the evolution of the He I IR line as a function of increasing activity, we took two best-fit models of

inactive stars from our previous work and varied their activity state. We thus included eight newly calculated models from series A and B in our investigation even though models B5 and B6 did not pass the Pa β criterion.

3. Results and discussion

3.1. Model EUV flux and its effect on the He I IR line

The wavelength range of the EUV is self-consistently calculated within the PHOENIX models according to the prescribed atmospheric structure. The maximum temperature is 98 000 K in all of our models. We did not extend the models to higher temperatures because then conduction plays a major role that is not incorporated in the PHOENIX models. In this regard, the models underpredict the EUV radiation field because the upper part of the transition region and the corona are neglected.

Andretta & Jones (1997) highlighted that it is important that the EUV radiation field is irradiated from the solar transition region and corona in the formation of the He I spectrum of the Sun. Omitting the radiation field in the VAL C model of the quiet Sun, the authors obtained a model spectrum without any visible He I line. We repeated this exercise exemplarily for one of our inactive models A2 and of our most active model B6, and show the resulting He I IR line in Fig. 4. While the original model spectra were calculated down to a wavelength of 10 Å, we cut off the wavelength range $\lambda \leq 504$ Å and left everything else unchanged. In the spectrum of the modified model A2, the He I IR line completely vanishes, while the self absorption of the fill-in seen in model B6 turns into a slight emission line without any sign of self-absorption. This indicates that in the PHOENIX model calculations the PR mechanism is important in populating the metastable 2^3S level of helium to obtain any absorption feature in the first place. Because the PR mechanism is eliminated in the modified model B6, the emission is caused by collisional excitation alone.

We calculated the emanating EUV radiation of our PHOENIX models by integrating the flux density in the wavelength range of $10 \text{ \AA} \leq \lambda \leq 504 \text{ \AA}$ (F_{EUV}) and related it to the integrated bolometric flux (F_{bol}). In Fig. 5 we show the pEW(He I IR) as a function of the EUV radiation field as measured by $F_{\text{EUV}}/F_{\text{bol}}$. The values of $F_{\text{EUV}}/F_{\text{bol}}$ from our non-flaring PHOENIX models (all models investigated in this work except for models B5 and B6) as shown in Fig. 5 range from 4.5×10^{-7} for model 047 to 1.48×10^{-4} for model A4. These values are difficult to compare to observations because EUV observations for M dwarfs are especially hard to come by. Nevertheless, we can compare our values to the estimated EUV radiation field of GJ 176 from Loyd et al. (2016), obtained in the context of the Measurements of the Ultraviolet Spectral Characteristics of Low-mass Exoplanetary Systems (MUSCLES) Treasury Survey. The estimated $F_{\text{EUV}}/F_{\text{bol}}$ value of GJ 176 from Loyd et al. (2016) is in the order of 10^{-5} , which is slightly higher than the typical value that we obtain for our nonflaring PHOENIX models; the median of $F_{\text{EUV}}/F_{\text{bol}}$ of the nonflaring models is 8.9×10^{-6} . GJ 176 is slightly above our effective temperature range with $T_{\text{eff}} = 3689 \pm 54$ K (Passegger et al. 2019). We therefore conclude that the calculated $F_{\text{EUV}}/F_{\text{bol}}$ values from our non-flaring PHOENIX chromospheres are compatible with observational results of EUV radiation, although our models neglect the temperature region of the upper transition and corona because of the model temperature limit of 98 000 K. However, compared to real stars, our models presumably contain too much material in the lower transition region, and this might therefore compensate

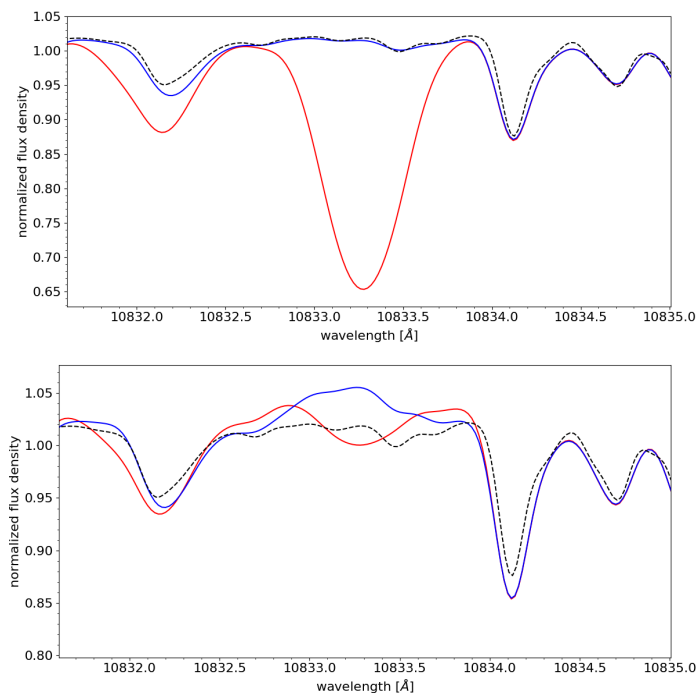


Fig. 4. Spectral ranges of the He I IR line in models A2 (*upper panel*) and B6 (*lower panel*) in the original configuration (red lines) and when the radiation field below 504 Å (blue lines) is omitted. The dashed black line shows the underlying photosphere alone (from Husser et al. (2013) with $T_{\text{eff}} = 3500$ K, $\log g = 5.0$ dex, $[\text{Fe}/\text{H}] = 0.0$ dex, and $[\alpha/\text{Fe}] = 0.0$ dex).

for the material that we omitted in the upper transition region and corona. This means that we obtain realistic $F_{\text{EUV}}/F_{\text{bol}}$ within our models despite this inadequacy. For a recent detailed analysis of a synthetic EUV PHOENIX spectrum computed for the inactive M dwarf Ross 905, we refer to the study by Peacock et al. (2019).

The graph in Fig. 5 shows that an increase in the strength of the radiation field in the transition region tends to deepen the He I IR line. The effect of the radiation field on the line strength decreases at higher irradiation levels. For $F_{\text{EUV}}/F_{\text{bol}} \lesssim 2.0 \times 10^{-5}$, absorption in the He I IR line strongly increases in response to a comparably weak rise of the integrated EUV flux. When the models are shifted farther inward, the EUV flux increases more strongly, but the He I IR line strength only changes slowly. The pEW(He I IR) seems to saturate or even starts to fill in for higher $F_{\text{EUV}}/F_{\text{bol}}$ values. Our modeling yields a maximum absorption depth at pEW = 0.35 Å for model 057.

The comparison of the results for series A and B shows that both series yield a qualitatively similar behavior within the low-activity regime of the pEW(He I IR) vs. $F_{\text{EUV}}/F_{\text{bol}}$ plane, although they differ in their model parameters such as the temperature gradient in the transition region. However, the extent of the response of the radiation field and the line depth on the shift of the models depends on the series. In both cases, the chromospheres are equal in thickness on the column mass density scale, but the gradients of the upper chromospheres and transition regions differ from each other. This difference affects the density at the temperatures where the PR mechanism works in the He I IR line formation. Fig. 5 shows that the effect of shifting the prescribed atmospheric structure in series B is stronger than in A. In model series A, the line absorption monotonically increases with increasing $F_{\text{EUV}}/F_{\text{bol}}$. In the other model series, model B4 exhibits the highest absorption level (pEW = 0.165 Å)

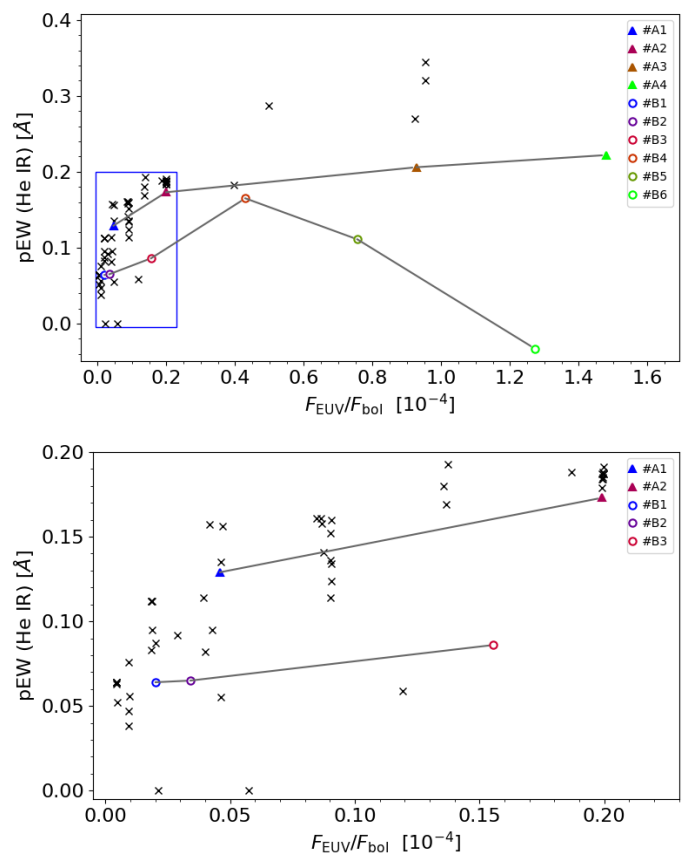


Fig. 5. He I IR pEW as a function of the integrated EUV flux at $\lambda \lesssim 504$ Å (vacuum). The color-coded models correspond to the new series A and B of models as given in Fig. 2. Black crosses represent the previously nonflaring models from Hintz et al. (2019) as given in Table A. The region marked by the blue rectangular in the *upper panel* is enlarged in the *lower panel* and shows our most quiescent models.

at $F_{\text{EUV}}/F_{\text{bol}} = 4.3 \times 10^{-5}$. A further inward shift results in filling in the line with a further increase in the radiation field. Because the maximum absorption depth is not reached for series A, the saturation level does not appear to be determined solely by the position of the chromospheric structure in the atmosphere, but also depends on other parameters such as temperature gradients or the temperature at the onset of the transition region.

3.2. Comparison to observations

Fuhrmeister et al. (2019) compared the pEW(He I IR) measurements of their investigated M-dwarf sample to X-ray observations that can serve as a proxy of the EUV radiation field. For their inactive and quiescent stars, they found that for low $\log L_X/L_{\text{bol}}$ values the full range of pEW(He I IR) values was observed. For high X-ray luminosities, only high pEW(He I IR) values were seen, that is, there is some sort of lower envelope that is correlated with $\log L_X/L_{\text{bol}}$. This lower envelope has the steepest gradient for M0 dwarfs, while later subtypes exhibit lower gradients, with M3–4 dwarfs showing no dependence on $\log L_X/L_{\text{bol}}$. For the M2–3 dwarfs considered here, they therefore only found a very weak tendency for high $\log L_X/L_{\text{bol}}$ values excluding low pEW(He I IR) values.

Our models, on the other hand, show a correlation between the pEW(He I IR) and $F_{\text{EUV}}/F_{\text{bol}}$ measurements. Nevertheless, this need not necessarily be a discrepancy. We do not know

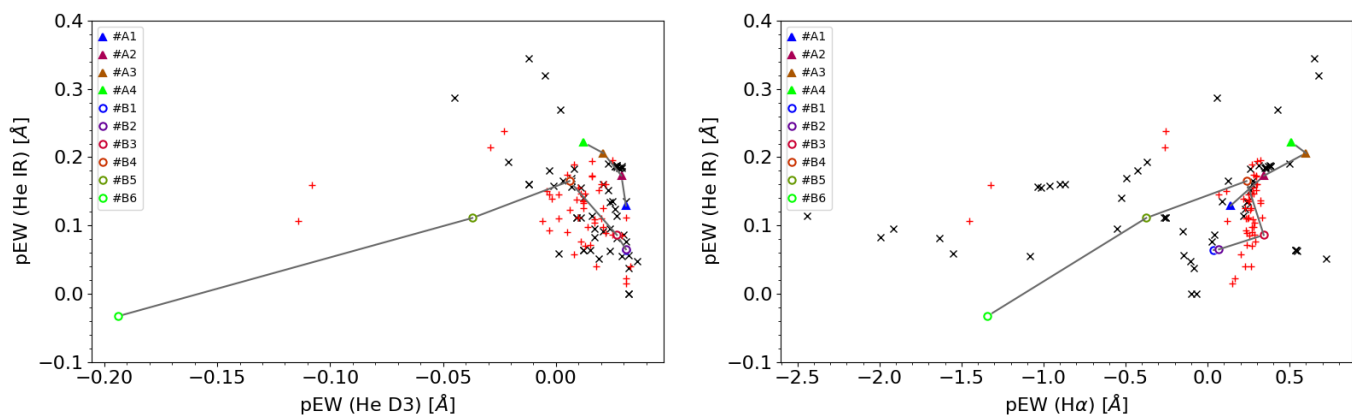


Fig. 6. pEWs of the He I IR line as a function of the pEWs of the He I D₃ (left panel), and H α (right panel) lines. Black crosses represent the nonflaring models from Hintz et al. (2019). Series A and B are depicted by color-coded squares (the color-coding corresponds to that of Fig. 2). CARMENES observations of the investigated M2–M3 V stars are flagged by red pluses. In the observed pEW(He I D₃) of the stellar sample, we add an offset of 0.06 Å because these measurements are influenced by a decline in flux in the respective normalization reference bands from the blue to the red continuum.

which $F_{\text{EUV}}/F_{\text{bol}}$ values the observations span, but when we take only the nonflaring measurements into account, they are probably covered by a subset of models from the zoom-in (lower panel in Fig. 5). When only the models with $0.04 \times 10^{-4} < F_{\text{EUV}}/F_{\text{bol}} < 0.1 \times 10^{-4}$ are considered, the situation starts to look similar to the observations: while the upper envelope of the pEW(He I IR) values is quite constant, the lower envelope shows some rise. Moreover, the spread in pEW(He I IR) seen for the models for a distinct $F_{\text{EUV}}/F_{\text{bol}}$ value should dilute a possible correlation even more in the observations because they are additionally prone to measurement errors, errors arising from using X-ray fluxes as approximation for F_{EUV} , and from nonsimultaneous measurements in X-ray and pEW(He I IR).

Nevertheless, Fuhrmeister et al. (2019) also found some saturation limit that depended on spectral type, which is about $\text{pEW}_{\text{sat}}=0.25$ Å for spectral types M2.0–2.5 V and $\text{pEW}_{\text{sat}}=0.2$ Å for M3.0–3.5 V stars. This agrees with the overall saturation limit found by the models, although individual models predict even deeper He I IR lines. The EUV radiation where the response of the He I IR line saturates in our model series B may be connected with a change in formation mechanism, that is, the collisional excitation becomes dominant because the models B5 and B6 are flare models and the observations by Fuhrmeister et al. (2019) with positive pEW(He I IR) are connected with flaring events. Omitting the EUV radiation in the models also supports this conclusion because an inactive chromosphere model without EUV radiation does not show any signal of the He I IR line, and an active model tends to show the He I IR line in emission.

3.3. He I IR in relation to other chromospheric lines

In Fig. 6 we show the pEW measurements of the stars and our models for the He I IR line as a function of pEW(He I D₃) and pEW(H α). The models show the He I IR line from the state of absorption to being indistinguishable from the surrounding photospheric background, which may indicate a very weak or a filled-in line. In the original model suite, the He I IR line emission is only found in combination with Pa β line emission, which led to their exclusion (Sect. 2.6). This is in line with observations, where He I IR line emission was observed during flares (Schmidt et al. 2012; Fuhrmeister et al. 2008).

In the measurements of the He I D₃ line we found an offset between the observations and the model values. The surrounding continua exhibit a decline from the blue to the red reference bands for the observations, which affects the normalization in the calculations of the pEW values of these lines. Therefore we added an offset of 0.06 Å to the pEW measurements of the observations. The behavior of the He I D₃ line is easiest to interpret because it only slightly starts to rise above the continuum with increasing depth of the He I IR line for the models as well as for the observations. The series of models created here also shows this trend for all models of series A and for models B1–B4, that is, for all the quiescent models of the new series. The flare models B5 and B6 show increasing fill-in of the He I IR line, while the line emission of He I D₃ strengthens further. The same applies to the two most active stars of the observed sample. Furthermore, within the inactive range of the models and observations, the He I IR sensitivity to the density shift is notably higher than that of the D₃ line. This is also confirmed by the respective line evolution shown in Fig. 3. This is in line with expectations because the lower level of the D₃ line is the upper level of the He I IR line. The population of the excited D₃ level lags the population of the excited He I IR level.

The H α line behavior in the models shows that no combination of a deep He I IR line and H α clearly in emission appears to be possible. Nevertheless, the model series A and B and the measurements of the observed stars show the same trend: H α behaves similarly to the He I IR line: first the line deepens before some fill-in begins that eventually drives the lines into emission.

We also studied the relationship of pEW(He I IR) to pEW(Na I D₂) and pEW(Ca II IRT). For these lines, the models seem to show no dependence on the pEW(He I IR). Nevertheless, the observations show that both lines only fill in with increasing activity. For a weak He I IR line, measurements of the Ca II IRT or Na I D₂ line therefore determine if the He I IR line is intrinsically weak or filled in.

For all lines, the observed pEW combinations are generally well reproduced by the models. Only the observations of the two active stars TYC 3529-1437-1 and LP 733-099 show a combination in the pEW(He I IR) versus pEW(He I D₃) plane that is not covered by the models. Furthermore, the models hardly reproduce the pEW measurements of the stars in the very inactive regime of the pEW(He I IR) versus pEW(H α) space. For some

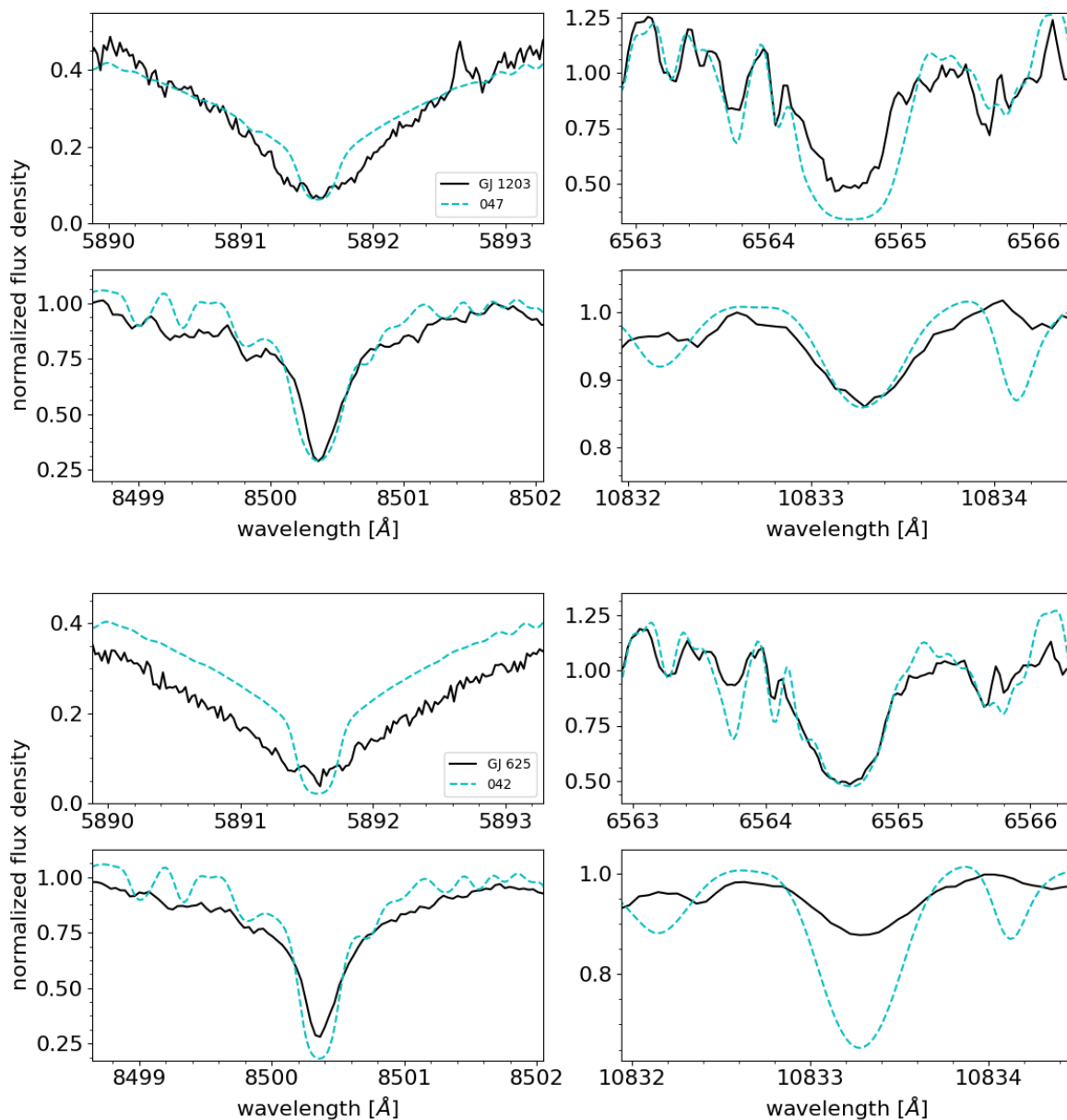


Fig. 7. *Upper panel:* Comparison of the best-fit model spectrum (dashed cyan line, model 047) to an observed spectrum (solid black line) of GJ 1203 optimized for the lines of Na I D₂ (*top left panel*), H α (*top right panel*), and the bluest Ca II IRT line (*bottom left panel*). In the range of the He I IR line (*bottom right panel*), the observed CARMENES template obtained with SERVAL is shown. The emission line redward of the Na I D₂ line in the observation of GJ 1203 is an airglow line. *Bottom panel:* Same as in the upper plot for GJ 625 (model 042).

discussion on these aspects, see Sect. 3.4. However, the quiescent models of series A and B mainly follow the observations of the inactive stars.

3.4. Predicting the He I IR line from previous best-fitting models

On the basis of the chromospheric modeling as done in Hintz et al. (2019), we here determined how well the models reproduce the He I IR line. In that study, only the Na I D₂, H α , and the bluest Ca II IRT line were used to identify best-fit models for all stars by minimizing a modified χ^2 value (χ_m^2) for these three lines.

Examples of the inactive stars (with single-model fits) can be found in Fig. 7 for GJ 1203 and GJ 625. Here we show the three lines that were used before and the predicted line shape of

the He I IR line, which is reproduced well for GJ 1203 and over-predicted for GJ 625. However, all of our best-fit models show the He I IR line in absorption and therefore reproduce this characteristic of the observed stellar sample. As an indicator for the goodness of the prediction of the respective models in the range of the He I IR line, we calculated reduced χ^2 values in the wavelength interval $10\,833.306 \pm 0.5$ Å ($\chi_{\text{He I IR}}^2$). The two different χ^2 quantities, $\chi_{\text{He I IR}}^2$ and χ_m^2 , are not directly comparable. Here we analyze the prediction of the modeled He I IR line, therefore we only compare the $\chi_{\text{He I IR}}^2$ values (see Table 2). From visual inspection, we specified a $\chi_{\text{He I IR}}^2 \leq 2$ to flag a model prediction of the He I IR line to be adequate for an observation. Approximately for half of the listed stars, the best-fit model prediction is appropriate according to this selection criterion. When the model pre-

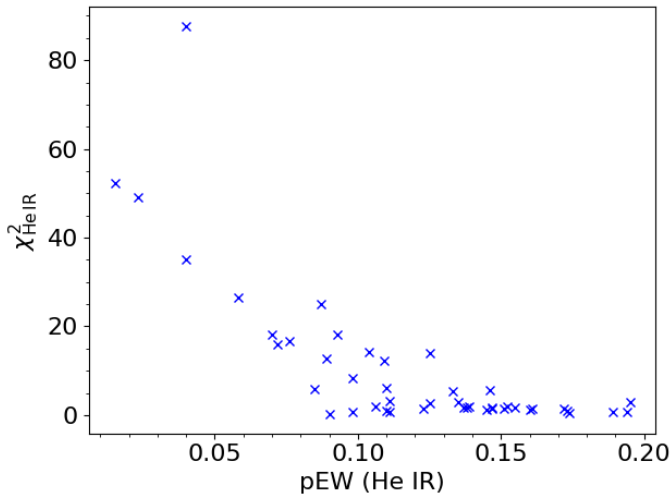


Fig. 8. Measurements of the pEW (He I IR) plotted against the corresponding $\chi^2_{\text{He I IR}}$ values for the inactive stars from Table 2.

diction strongly differs, that is, $\chi^2_{\text{He I IR}} > 10$, the He I IR line absorption is clearly overpredicted, as shown in Fig. 7 for GJ 625.

Because Hintz et al. (2019) identified only five best-fit models in their the whole sample of inactive stars in our previous study, we now determine which of those five models describes the He I IR line best and then recompute the χ^2_m values for this model. These results are shown in Table 2. The He I IR line is best predicted by models 029 and 047 for all but three stars. These models in many cases describe the He I IR line better and show only a marginally worse new χ^2_m value. A prominent example is GJ 3452. On the other hand, the description of the two most inactive stars, Ross 730 and HD 349726, within the He I IR line is poor for any of the five best-fit models. This leads us to the general assumption that the He I IR line prediction becomes worse when the line is shallow, as is shown in Fig. 8. This may be caused by a lack of appropriate inactive models in our model suite or may indicate that our ansatz with a 100% filling factor for the chromospheres fails and even atmospheres of the most inactive stars are partially filled with plage regions. The cases for which the original best fits already yield an adequate He I IR line description can by construction lead to an even better description, but it considerably worsens the χ^2_m in most cases. This shows that more than one individual line needs to be used for chromospheric model fitting, as reported by Hintz et al. (2019).

Hintz et al. (2019) found that in the case of the active stars, linear-combination fits of two models (one inactive and one more active model) were necessary to obtain appropriate models. In Fig. 9 we illustrate the best linear combination fit for TYC 3529-1437-1. In the combination fits of the active stars, the line in the active component tends to go into emission, but the combination still shows the He I IR line in absorption. Table 3 lists our information about the He I IR line prediction of the combination fits of the active stars. Interestingly, the He I IR line can be well reproduced by the best-fit model combinations without including this line in the fitting procedure, as is evident from the $\chi^2_{\text{He I IR}}$ values.

4. Summary and conclusions

We presented a theoretical study of the He I IR line in M2–3 V stars with PHOENIX. Our study was based on a set of chromospheric PHOENIX models computed in our previous study,

Table 2. Best-fit models for the inactive stars from Table A.1 of Hintz et al. (2019) and the calculated reduced χ^2 value (Col. 4) in the He I IR line.

Stars	Model	χ^2_m	$\chi^2_{\text{He I IR}}$	Model ^a	χ^2_m ^a	$\chi^2_{\text{He I IR}}$ ^a
Wolf 1056	047	2.75	1.80	029	4.73	0.62
GJ 47	047	2.53	1.79	029	4.14	0.38
BD+70 68	080	2.26	0.72	079	2.74	0.72
GJ 70	079	2.29	1.95	029	4.85	0.41
G 244-047	042	3.45	5.73	029	4.22	0.95
VX Ari	079	3.61	6.10	047	4.11	0.73
Ross 567	042	2.75	18.21	047	3.26	0.49
GJ 226	047	1.80	1.67	029	4.52	0.48
GJ 258	047	3.83	1.36	029	5.27	0.46
GJ 1097	042	4.04	12.79	047	4.34	0.47
GJ 3452	042	2.37	18.09	047	2.99	0.33
GJ 357	042	2.63	35.03	047	3.25	1.85
GJ 386	047	2.78	1.51	029	4.00	0.78
LP 670-017	080	4.51	5.92	047	4.53	0.37
GJ 399	079	2.54	1.89	029	5.10	0.62
Ross 104	079	2.59	2.58	029	4.44	0.46
Ross 905	042	2.84	12.23	047	2.94	0.75
GJ 443	080	2.04	1.39	029	7.48	0.74
Ross 690	079	2.41	5.27	047	2.81	1.31
Ross 695	042	2.91	87.59	047	3.16	5.80
Ross 992	079	2.85	1.67	029	5.18	0.42
θ Boo B	047	2.55	0.78	047	2.55	0.78
Ross 1047	047	3.16	0.94	029	4.41	0.72
LP 743-031	080	3.38	14.27	047	4.69	0.97
G 137-084	080	2.66	1.96	029	4.97	0.36
EW Dra	080	2.31	0.46	080	2.31	0.46
GJ 625	042	2.41	25.02	047	2.43	0.63
GJ 1203	047	2.50	0.24	047	2.50	0.24
LP 446-006	047	2.82	1.11	029	3.72	1.03
Ross 863	079	3.11	3.08	029	4.02	0.60
GJ 2128	042	2.45	16.69	047	2.58	0.41
GJ 671	042	3.30	15.92	047	3.55	0.31
G 204-039	080	2.79	1.34	029	5.82	0.38
Ross 145	042	3.28	26.56	047	4.19	0.71
G 155-042	042	3.54	8.40	047	3.56	0.76
Ross 730	029	2.82	52.27	047	6.02	15.92
HD 349726	029	2.83	49.21	047	5.61	14.22
GJ 793	080	3.01	1.17	029	7.02	0.37
Wolf 896	047	2.59	2.83	079	2.66	0.73
Wolf 906	079	2.43	0.92	029	5.29	0.65
LSPM J2116						
+0234	079	3.08	1.54	029	5.10	0.57
BD-05 5715	080	2.90	0.69	080	2.90	0.69
Wolf 1014	042	3.32	13.91	047	4.21	0.94
G 273-093	047	1.97	0.74	047	1.97	0.74
Wolf 1051	080	2.31	2.94	029	6.39	0.68

^a Columns 5–7 list the results of the model with the best He I IR line prediction within the subsample of the five best-fitting models for the inactive stars. For stars whose original model already resulted in an adequate description of the He I IR line, we mark the He I IR line best-fit model in gray.

Hintz et al. (2019), and new systematic series of chromospheric models. Following the approach of previous M-dwarf star studies, all our models (previous and new models) were created by parameterizing the semiempirical solar VAL C temperature structure. The model spectra were then used to fit observed CARMENES spectra of M2–3 V stars in the Na I D₂, H α , and the bluest Ca II IRT lines. A statistical analysis reveals the best fits. Here, we extended the study to investigate the behavior of the He I IR line.

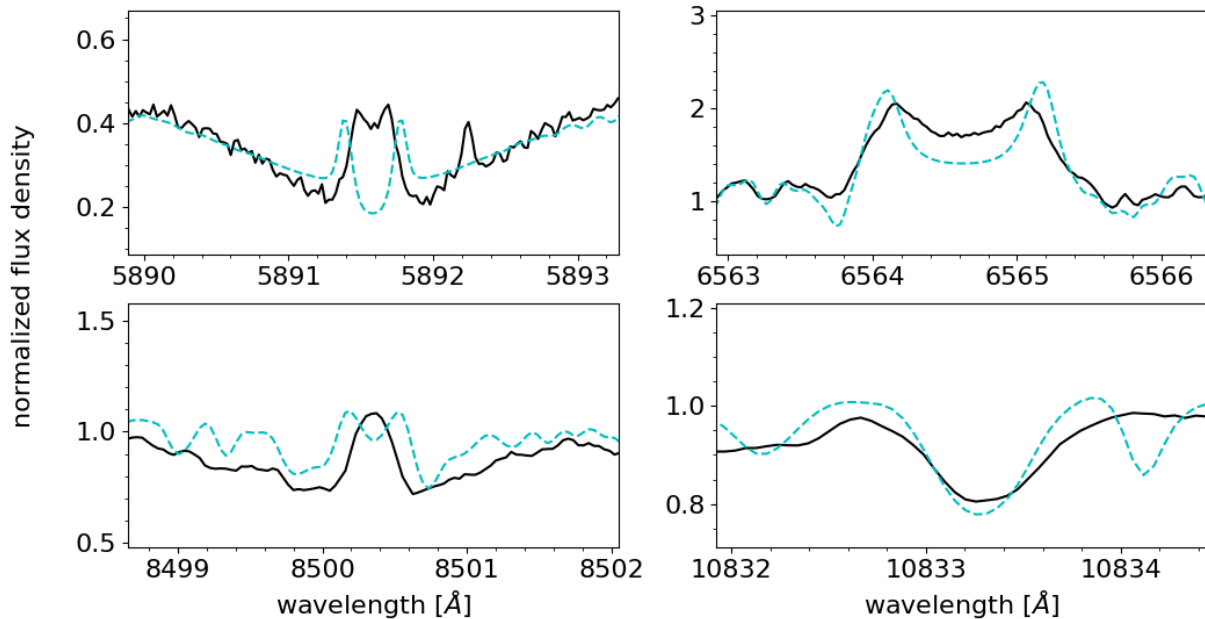


Fig. 9. Comparison of the best linear combination fit (dashed cyan line, from Hintz et al. (2019)) to an observed spectrum (solid black) TYC 3529-1437-1 optimized for the lines of Na I D₂ (top left panel), H α (top right panel), and the bluest Ca II IRT line (bottom left panel) and extended to the He I IR line (bottom right panel). The linear combination consists of 74.9% of inactive model 079 and 25.1% of active model 149.

Table 3. Best-fit models of the active stars in a linear-combination fit with filling factors (FF) and the calculated χ^2 value (Col. 5) in the He I IR line.

Stars	Inactive model	FF	Active model	FF	χ_m^2	$\chi_{\text{He I IR}}^2$
G 234-057	080	0.90	139	0.10	3.58	1.54
GJ 360	080	0.82	132	0.17	5.13	0.70
LP 733-099	079	0.68	149	0.32	16.13	0.48
TYC 3529-1437-1	079	0.75	149	0.25	14.25	0.50

Our new model series were computed by shifting an inactive model structure in column mass density. In these series, denser chromospheres correspond to higher activity levels. From low to high activity levels, our models predict that the He I IR line first goes into absorption and then reaches a maximum depth, after which fill-in sets in. Our models reproduce the point of maximum He I IR line absorption at $\sim 300 \text{ m}\text{\AA}$. The H α line shows the same qualitative behavior, but reaches the turning point at lower activity levels. In contrast, the Na I D₂ and the bluest Ca II IRT lines only show fill-in with increasing activity levels. Furthermore, the He I D₃ line never shows absorption in our models, but directly goes into emission with increasing activity levels.

By investigating the He I IR line as a function of the EUV radiation field arising from the models themselves, we find that the most inactive models are highly sensitive to an increase in EUV radiation, which produces a strong rise in the pEW(He I IR). With further increases of the EUV radiation, the line absorption tends to saturate. The detailed response of the radiation field and the He I IR line to density shifts of the atmospheric structure depends on the configuration of the chromosphere.

Suppressing EUV emission and thus the PR mechanism altogether, we showed that collisional excitation gains in importance

for the formation of the He I IR line as activity levels increase beyond the point of maximum He I IR line absorption. Our investigation of chromosphere models showed that the PR mechanism and collisional excitation both contribute to the He I IR formation, with the PR mechanism dominating the low-activity regime. This is in line with former results on the He I IR line formation in the Sun.

The whole stellar comparison sample shows the He I IR line in absorption. We showed that the best-fit models for inactive stars selected by Hintz et al. (2019) based on optical activity indicators often also predict the He I IR line quite well. In other cases, an appropriate inactive model can be found that fits both the optical and He I IR lines well. For active stars, a linear combination of an active and inactive component is required to obtain a good approximation, as reported in Hintz et al. (2019).

Our current study demonstrates that one-dimensional PHOENIX model atmospheres with a parameterized temperature structure reproduce the observed behavior of the He I IR line in M2–3 V stars. Its strong response to EUV irradiation in the low-activity regime makes the He I IR line a promising proxy of this otherwise inaccessible wavelength range there. The comparably weak response of the line to changes in the EUV radiation field that start already at moderate activity levels is favorable for planetary transmission spectroscopy of active stars, where constant reference spectra are crucial.

Acknowledgements. CARMENES is an instrument for the Centro Astronómico Hispano-Alemán de Calar Alto (CAHA, Almería, Spain). CARMENES is funded by the German Max-Planck-Gesellschaft (MPG), the Spanish Consejo Superior de Investigaciones Científicas (CSIC), the European Union through FEDER/ERF FICTS-2011-02 funds, and the members of the CARMENES Consortium (Max-Planck-Institut für Astronomie, Instituto de Astrofísica de Andalucía, Landessternwarte Königstuhl, Institut de Ciències de l’Espai, Institut für Astrophysik Göttingen, Universidad Complutense de Madrid, Thüringer Landessternwarte Tautenburg, Instituto de Astrofísica de Canarias, Hamburger Sternwarte, Centro de Astrobiología and Centro Astronómico Hispano-Alemán), with additional contributions by the Spanish Ministry of Sci-

ence [through projects AYA2016-79425-C3-1/2/3-P, ESP2016-80435-C2-1-R, AYA2015-69350-C3-2-P, and AYA2018-84089], the German Science Foundation through the Major Research Instrumentation Programme and DFG Research Unit FOR2544 “Blue Planets around Red Stars”, the Klaus Tschira Stiftung, the states of Baden-Württemberg and Niedersachsen, and by the Junta de Andalucía. D.H. acknowledges funding by the DLR under DLR 50 OR1701. B.F. acknowledges funding by the DFG under Cz 222/1-1 and Schm 1032/69-1. S.C. acknowledges support through DFG projects SCH 1382/2-1 and SCHM 1032/66-1. We thank the anonymous referee for the comprehensive review.

References

- Andretta, V. & Giampapa, M. S. 1995, *ApJ*, 439, 405
 Andretta, V. & Jones, H. P. 1997, *ApJ*, 489, 375
 Avrett, E. H., Fontenla, J. M., & Loeser, R. 1994, in *IAU Symposium*, Vol. 154, *Infrared Solar Physics*, ed. D. M. Rabin, J. T. Jefferies, & C. Lindsey, 35
 Ayres, T. R. 1979, *ApJ*, 228, 509
 Caballero, J. A., Guàrdia, J., López del Fresno, M., et al. 2016, in *Proc. SPIE*, Vol. 9910, *Observatory Operations: Strategies, Processes, and Systems VI*, 99100E
 Fuhrmeister, B., Czesla, S., Hildebrandt, L., et al. 2019, *A&A*, 632, A24
 Fuhrmeister, B., Liefke, C., Schmitt, J. H. M. M., & Reiners, A. 2008, *A&A*, 487, 293
 Hauschildt, P. H. 1992, *J. Quant. Spectr. Rad. Transf.*, 47, 433
 Hauschildt, P. H. 1993, *J. Quant. Spectr. Rad. Transf.*, 50, 301
 Hauschildt, P. H. & Baron, E. 1999, *Journal of Computational and Applied Mathematics*, 109, 41
 Hintz, D., Fuhrmeister, B., Czesla, S., et al. 2019, *A&A*, 623, A136
 Husser, T.-O., Wende-von Berg, S., Dreizler, S., et al. 2013, *A&A*, 553, A6
 Leenaarts, J., Golding, T., Carlsson, M., Libbrecht, T., & Joshi, J. 2016, *A&A*, 594, A104
 Liebert, J., Kirkpatrick, J. D., Reid, I. N., & Fisher, M. D. 1999, *ApJ*, 519, 345
 Loyd, R. O. P., France, K., Youngblood, A., et al. 2016, *ApJ*, 824, 102
 Nagel, E. 2019, PhD thesis, University of Hamburg
 Nortmann, L., Pallé, E., Salz, M., et al. 2018, *Science*, 362, 1388
 Passegger, V. M., Schweitzer, A., Shulyak, D., et al. 2019, *A&A*, 627, A161
 Paulson, D. B., Allred, J. C., Anderson, R. B., et al. 2006, *PASP*, 118, 227
 Peacock, S., Barman, T., Shkolnik, E. L., et al. 2019, *ApJ*, 886, 77
 Quirrenbach, A., Amado, P. J., Ribas, I., et al. 2018, in *Society of Photo-Optical Instrumentation Engineers (SPIE) Conference Series*, Vol. 10702, *Society of Photo-Optical Instrumentation Engineers (SPIE) Conference Series*, 107020W
 Salz, M., Czesla, S., Schneider, P. C., et al. 2018, *A&A*, 620, A97
 Sanz-Forcada, J. & Dupree, A. K. 2008, *A&A*, 488, 715
 Schmidt, S. J., Kowalski, A. F., Hawley, S. L., et al. 2012, *ApJ*, 745, 14
 Spake, J. J., Sing, D. K., Evans, T. M., et al. 2018, *Nature*, 557, 68
 Takeda, Y. & Takada-Hidai, M. 2011, *PASJ*, 63, 547
 Vaughan, Jr., A. H. & Zirin, H. 1968, *ApJ*, 152, 123
 Vernazza, J. E., Avrett, E. H., & Loeser, R. 1981, *ApJS*, 45, 635
 Zarro, D. M. & Zirin, H. 1986, *ApJ*, 304, 365
 Zechmeister, M., Reiners, A., Amado, P. J., et al. 2018, *A&A*, 609, A12
 Zirin, H. 1975a, *NASA STI/Recon Technical Report N*, 76
 Zirin, H. 1975b, *ApJ*, 199, L63

Appendix A: Reviewed former model set

Here, we list the parameters of the models from Hintz et al. (2019) that we review in this work according to our selection criteria in Sect. 2.6. The non-listed models either show the line of Pa β in obvious emission or their onset of the transition region falls below a temperature of $T_{\text{top}} = 6000$ K.

Table A.1. Reviewed former model set and parameters from Table C.1 in Hintz et al. (2019) for the models that fulfill our selection criteria as described in Sect. 2.6.

Model	m_{min} [dex]	m_{mid} [dex]	T_{mid} [K]	m_{top} [dex]	T_{top} [K]	∇_{TR} [dex]
001	-4.0	-4.3	5500	-6.0	6000	7.5
005	-3.5	-3.8	5500	-5.5	6000	7.5
009	-3.2	-3.6	5500	-5.1	6000	7.5
014	-3.1	-3.3	5500	-5.0	6000	8.5
016	-3.0	-3.6	5500	-5.0	6000	7.5
020	-3.0	-3.3	5500	-5.0	6000	7.5
021	-3.0	-3.3	5500	-5.0	6000	7.5
023	-2.8	-3.6	5500	-5.0	6000	7.5
025	-2.8	-3.3	5500	-5.0	6000	7.5
028	-2.6	-3.2	4500	-4.5	6000	8.5
029	-2.6	-3.2	4500	-4.5	7000	8.5
031	-2.6	-3.0	4500	-4.5	6000	8.5
032	-2.6	-3.0	4500	-4.5	7000	8.5
037	-2.6	-2.8	4500	-4.5	6000	8.5
038	-2.6	-2.8	4500	-4.5	7000	8.5
040	-2.5	-3.6	5500	-5.0	6000	7.5
041	-2.5	-3.6	5500	-5.0	6200	7.5
042	-2.5	-3.6	5500	-5.0	6500	7.5
044	-2.5	-3.3	5500	-5.0	6000	7.5
046	-2.5	-2.8	5500	-4.5	6000	7.5
047	-2.5	-2.7	6500	-5.0	7000	9.2
049	-2.1	-2.6	6500	-4.5	7000	7.5
050	-2.1	-2.6	6500	-4.0	7000	9.2
055	-2.1	-2.3	5000	-4.0	6000	9.5
056	-2.1	-2.3	5500	-5.0	6000	7.5
057	-2.1	-2.3	5500	-4.5	6000	7.5
059	-2.1	-2.3	5500	-4.0	6000	9.5
060	-2.1	-2.3	6500	-5.0	7000	9.2
061	-2.1	-2.3	6500	-4.5	7000	9.2
062	-2.1	-2.3	6500	-4.2	7000	8.2
063	-2.1	-2.3	6500	-4.0	7000	9.0
064	-2.1	-2.3	6500	-4.0	7000	9.2
065	-2.0	-2.5	6500	-5.0	8000	9.2
066	-2.0	-2.5	6500	-4.5	8000	9.2
068	-2.0	-2.3	6500	-5.0	7000	9.2
069	-2.0	-2.3	6500	-4.5	7000	9.2
070	-2.0	-2.3	6500	-4.0	7000	9.2
071	-2.0	-2.2	6500	-5.0	7000	9.2
072	-2.0	-2.2	6500	-4.5	7000	9.2
073	-1.9	-2.3	6500	-4.0	7000	9.2
078	-1.8	-2.3	6500	-4.0	7000	9.0
079	-1.5	-2.5	5000	-4.0	7500	8.5
080	-1.5	-2.5	5500	-4.0	7500	8.5
081	-1.5	-2.5	6000	-4.1	7500	8.5
083	-1.5	-2.5	6000	-4.0	7500	8.5
095	-1.5	-2.3	6500	-4.5	7000	9.0
096	-1.5	-2.3	6500	-4.5	8000	9.2
097	-1.5	-2.3	6500	-4.0	7000	9.0
107	-1.0	-3.5	4000	-5.0	8000	9.5
108	-1.0	-3.5	4000	-4.5	8000	9.5
109	-1.0	-3.0	4000	-5.0	8000	9.5
110	-1.0	-3.0	4000	-4.5	8000	9.5
111	-1.0	-3.0	4000	-4.0	8000	9.5
124	-1.0	-2.5	4000	-4.0	8000	9.5
131	-1.0	-2.5	5200	-3.7	8000	9.5
152	-1.0	-2.0	4000	-4.0	8000	9.5
155	-1.0	-1.5	4000	-4.0	8000	9.5
159	-0.3	-3.0	4000	-4.5	8000	9.5